Journal of Alloys and Compounds 509 (2011) 7259–7266

Contents lists available at ScienceDirect

Journal of Alloys and Compounds

journal homepage: www.elsevier.com/locate/jallcom

Room temperature ferromagnetism in Mn-doped zinc oxide nanorods prepared by hybrid wet chemical route

M.K. Sharma [a], R.N. Gayen [b], A.K. Pal [b,*], D. Kanjilal [c], Ratnamala Chatterjee [a]

[a] Department of Physics, Indian Institute of Technology Delhi, New Delhi 110016, India
[b] Department of Instrumentation Science, USIC Building, Jadavpur University, Calcutta 700 032, India
[c] Inter University Accelerator Centre, Aruna Asaf Ali Marg, New Delhi 110067, India

ARTICLE INFO

Article history:
Received 5 February 2011
Received in revised form 5 April 2011
Accepted 5 April 2011
Available online 12 April 2011

PACS:
75.70.−i
75.50.Pp
81.07.Bc

Keywords:
Mn-doped ZnO
Room temperature ferromagnetism
Magnetic impurity
Nanostructure

ABSTRACT

Mn-doped (2.6–4.8 at%) aligned zinc oxide (Mn:ZnO) nanorod-films were synthesized by hybrid wet chemical route onto glass substrates. The chemical composition, structural, microstructural and magnetic studies were performed to investigate the origin of observed room temperature ferromagnetism (~0.11 μ_B/Mn) in these Mn doped ZnO nanorod-films. XPS studies indicated that incorporated Mn was in Mn^{2+} and Mn^{4+} states. Mn^{2+} atomic concentration was found to be significantly larger than Mn^{4+} concentration in all the samples. Disappearance of the Raman peak at ~577 cm^{-1} arising due to the Zn interstitials may be related to the substitution of Mn^{2+} in the Zn^{2+} site with annealing. Thus, Mn metal inclusions as Mn^{2+} in the ZnO lattice are possibly responsible for such large magnetic moment in the films.

1. Introduction

Transition metal doped ZnO has emerged as an attractive candidate for DMS material based on both theoretical [1,2] and experimental [3,4] studies. In particular, incorporation of Mn^{2+} into the large band gap ZnO lattice promises to lead to new magnetic, transport and optical properties in ZnO. For this purpose, Mn:ZnO compounds with predicted above-room-temperature ferromagnetism have attracted attention as promising spintronic materials [1]. These compounds have been mainly grown by pulsed laser deposition (PLD) [5], CVD [6], molecular beam epitaxy (MBE) [7,8], isothermal sintering [9,10], sol-gel method [11] or RF magnetron sputtering [12]. However, the origin of the ferromagnetism still remains controversial [13] as to whether it arises from manganese oxide, precipitation of secondary phase, or the replacement of Zn^{2+} by Mn^{2+} in the ZnO host lattice.

Currently, capability of depositing ZnO in different configurations [14–16] e.g. nanorods, nanobelts, nanowires (NWs), nanoneedles, nanotetrapods and nanocombs have been reported. Of all the structures, vertically aligned ZnO nanorods offer unique opportunity of modulating the physical properties by changing the aspect ratio and/or the number density of the ZnO nanorods. Not many studies on magnetic measurements on Mn-doped vertically aligned ZnO nanorods have been reported so far. Hence, studies on Mn-doped vertically aligned ZnO nanorods may open up a new avenue for exploiting this material for device applications [1,17,18].

In this communication, we present our studies on the magnetic properties of Mn-doped vertically aligned ZnO nanorods deposited by hybrid wet chemical route on glass substrate. The films were characterized by measuring structural, microstructural, magnetic properties, X-ray photoelectron spectroscopy and Raman properties.

2. Experimental procedures

Vertically aligned ZnO nanorods were deposited by wet chemical route onto glass substrates on which ZnO seed particles were pre-deposited by sputtering technique. Thus, this technique is essentially a hybrid technique where one may easily manipulate the size and distribution of the ZnO seed crystallites modulating the growth of ZnO nanorods. Details of the synthesis of the above ZnO nanorods were reported elsewhere [16]. Here we deposited ZnO nanorods for a fixed duration of 45 min.

Mn was evaporated from a tantalum boat at a system pressure ~10^{-6} mbar onto the above vertically aligned ZnO nanorods. The amount of manganese was controlled and recorded by a quartz crystal thickness monitor. Mn was deposited on the ZnO nanorods for three different durations so as to deposit Mn layer with thickness ~3 nm, 6 nm and 10 nm, keeping the rate of Mn evaporation fixed at ~0.2 nm/s. The

* Corresponding author. Tel.: +91 33 24146321; fax: +91 33 24146584.
E-mail address: msakp2002@yahoo.co.in (A.K. Pal).

0925-8388/$ – see front matter © 2011 Elsevier B.V. All rights reserved.
doi:10.1016/j.jallcom.2011.04.034

ZnO nanorods containing manganese, thus obtained, were then subjected to rapid thermal annealing (RTA) in argon atmosphere. The temperature of annealing was 773 K and duration was 3 min.

An FEI Quanta 200 scanning electron microscopy (SEM) was used to record the surface morphology at an operating voltage of 25 kV in back scatter mode. A Rigaku MiniFlex X-ray diffraction (XRD) using Cu K_α radiation was used to obtain the micro-structural information. Raman spectra were recorded using Renishaw inVia micro-Raman spectrometer using 514 nm Argon laser. The XPS spectra were recorded using a VG Microtech at a base pressure $\sim 10^{-10}$ mbar. The XPS setup used here is incorporated with a dual anode Mg–Al X-ray source with a hemispherical analyzer and a channeltron detector with a resolution 1.3 eV. The analyzer was operated with pass energy of 200 eV for large size survey scan of 0–1000 eV binding energy region. For high resolution scans pass energy of 20 eV was utilized. Monochromatic Mg K_α radiation (1256.6 eV) was used at 300 W for all the XPS measurements reported here. The system is equipped with an EX03 Ar ion sputtering gun for sample etching. Data analysis was done using VGX900 software incorporated with system while baseline correction was made by removing the Shirely background from all the spectra. The FWHM was measured from Gaussian Laurentzian fitting of the spectra. Concentration values were obtained by integrating the intensities of the XPS core level peaks and correcting for the Relative atomic sensitivity factors (RASF).

For investigation of magnetic properties of the films, temperature-dependent magnetization (M–T) and magnetic hysteresis (M–H) curves were measured using a superconducting quantum interference device (SQUID) magnetometer (Quantum Design, MPMSXL). M–T curves were measured both in zero-field-cooled (ZFC) and in field-cooled (FC) mode at the applied fields of 20 Oe, 100 Oe, and 500 Oe and M–H curves at 35 K and 300 K were measured in the field range $-5000\,\text{Oe} \le H \le 5000\,\text{Oe}$. The magnetic fields of 20 Oe, 100 Oe, and 500 Oe were applied in parallel as well as perpendicular to the substrate of the annealed Mn-doped ZnO nanorod films and measurements were carried out in both the configurations.

3. Results and discussion

3.1. Microstructural analysis

Fig. 1(a) and (b) shows the SEM micrographs and the corresponding XRD patterns of a representative film of ZnO nanorods and as-deposited film of Mn (3 nm): ZnO nanorods, respectively. It is observed that ZnO films deposited on glass substrate are mostly vertically aligned (Fig. 1(a)). Some of them could be seen to deviate from perfect vertical alignment. The corresponding XRD pattern indicates the evolution of oriented and aligned ZnO nanorods with the presence of a very strong characteristic peak located at $2\theta = 34.6^\circ$ for reflections from (0 0 2) planes. There are two very low intensity peaks located at $2\theta = 63.3^\circ$ and $2\theta = 73.5^\circ$ arising from reflections for (1 0 3) and (0 0 4) planes, respectively, of ZnO nanorods. Fig. 1(b) shows the morphology of the same film of ZnO nanorods with as-deposited Mn (3 nm thick) on it. It may be observed that the tips of the ZnO nanorods appear like inverted tear drops as Mn adatoms tried to trickle down the nanorods. The XRD pattern did not indicate any significant characteristic peak for Mn. When these as-deposited Mn:ZnO nanorods are subjected to rapid thermal annealing at 773 K for 3 min, Mn gets dispersed in ZnO matrix uniformly, possibly due to substitution of Zn by Mn atoms without affecting the observed alignment of the ZnO nanorods (Fig. 2(a)–(c)). This is true for all the films of ZnO nanorods deposited with increasing amount of Mn in them. Incorporation of Mn in ZnO lattice will be more apparent from the XRD patterns of the annealed Mn:ZnO nanorods as shown also in Fig. 2(d)–(f) which contains no observable peak for Mn after annealing. This would mean that annealing of Mn film at 737 K did not crystallize the Mn film but rendered Mn to go into ZnO lattice. The SEM pictures of three such Mn: ZnO nanorods with different amounts of Mn in them are shown in Fig. 2(a)–(c). Heights and widths of the nanorods were estimated from the lateral view of the above discussed SEM pictures taken at a tilt angle of 30°. Average length and diameter of the nanorods were ascertained by measuring the same for a large number of nanorods constituting the films. The average diameter and length of the nanorods obtained as above were ~80 nm and ~780 nm, respectively. Thus, the average aspect ratio of the nanorods will be ~9.75. Lattice constants, a and c, of

Table 1
Calculated lattice parameters (in nm), percentage of Mn^{2+}, Mn/Zn ratio and coercive field (H) for Mn:ZnO nanorod-films.

Sample name	Lattice constants (nm)	Mn^{2+}/Mn^4	Mn/Zn	H_{C+}(Oe) (35 K)	H_{C-}(Oe) (35 K)	$\Delta H = (H_{C+} - H_{C-})$ (35 K)	H_{C+}(Oe) (300 K)	H_{C-}(Oe) (300 K)	$\Delta H = (H_{C+} - H_{C-})$ (300 K)
ZnO	$a \sim 0$ .32485$c \sim 0.51875$								
Mn:ZnO (Mn ~ 2.6 at%)	$a \sim 0$ .32585$c \sim 0.51934$	1.25	0.133	114.3	112.3	2.0	84.9	81.6	3.3
Mn:ZnO (Mn ~ 4.3 at%)	$a \sim 0$ .32608$c \sim 0.51952$	1.45	0.194	134.8	132.8	2.0	92.3	88.8	3.5
Mn:ZnO (Mn ~ 4.8 at%)	$a \sim 0$ .32674$c \sim 0.51964$	1.52	0.244	172.2	170.1	2.1	103.8	99.8	4.0

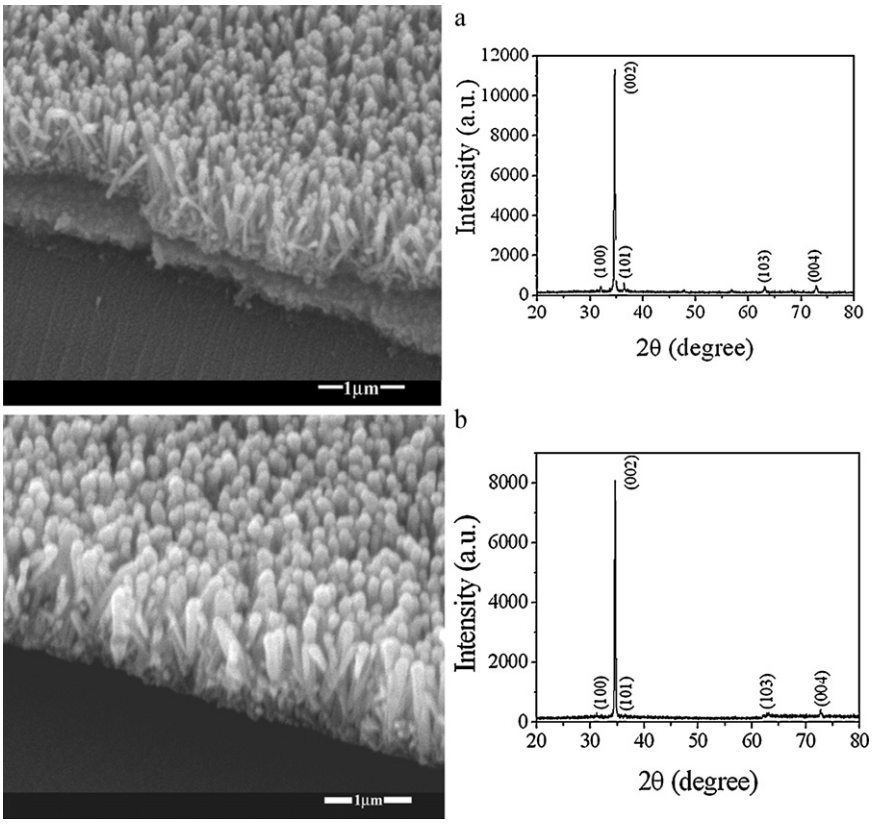

Fig. 1. SEM pictures and corresponding XRD patterns of a representative: (a) ZnO-nanorods and (b) ZnO with as-deposited Mn (3 nm).

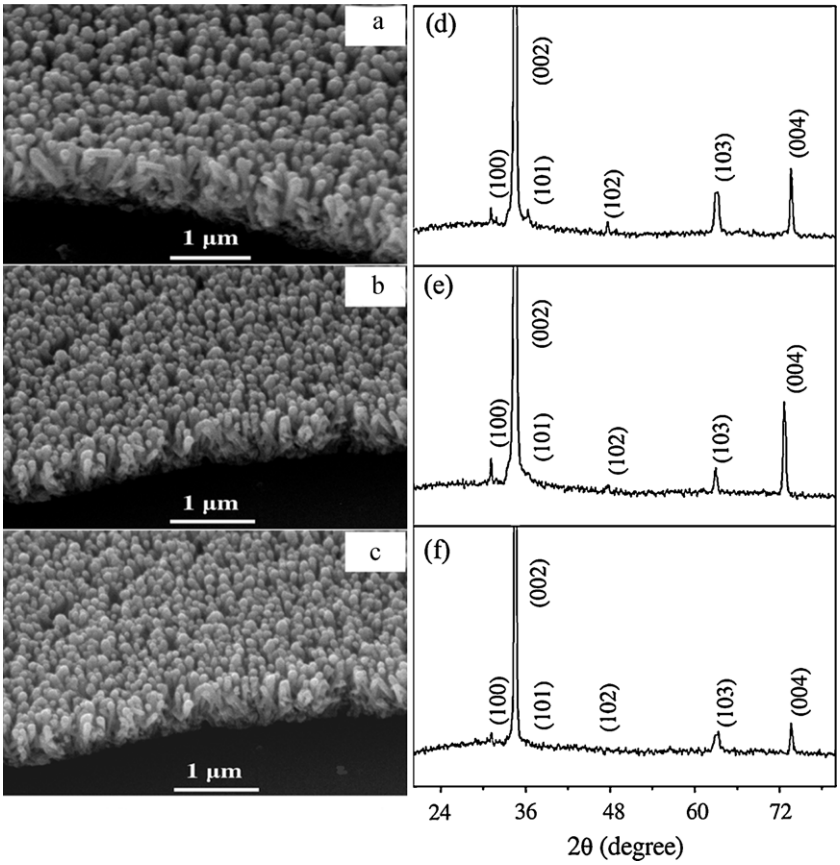

Fig. 2. SEM pictures of ZnO nanorods with different amounts of Mn after subjecting them to RTA: (a) Mn:ZnO (Mn ~ 2.6 at%); (b) Mn:ZnO (Mn ~ 4.3 at%) and (c) Mn:ZnO (Mn ~ 4.8 at%) and the corresponding XRD patterns of the Mn:ZnO nanorods: (d) Mn:ZnO (Mn ~ 2.6 at%); (e) Mn:ZnO (Mn ~ 4.3 at%) and (f) Mn:ZnO (Mn ~ 4.8 at%).

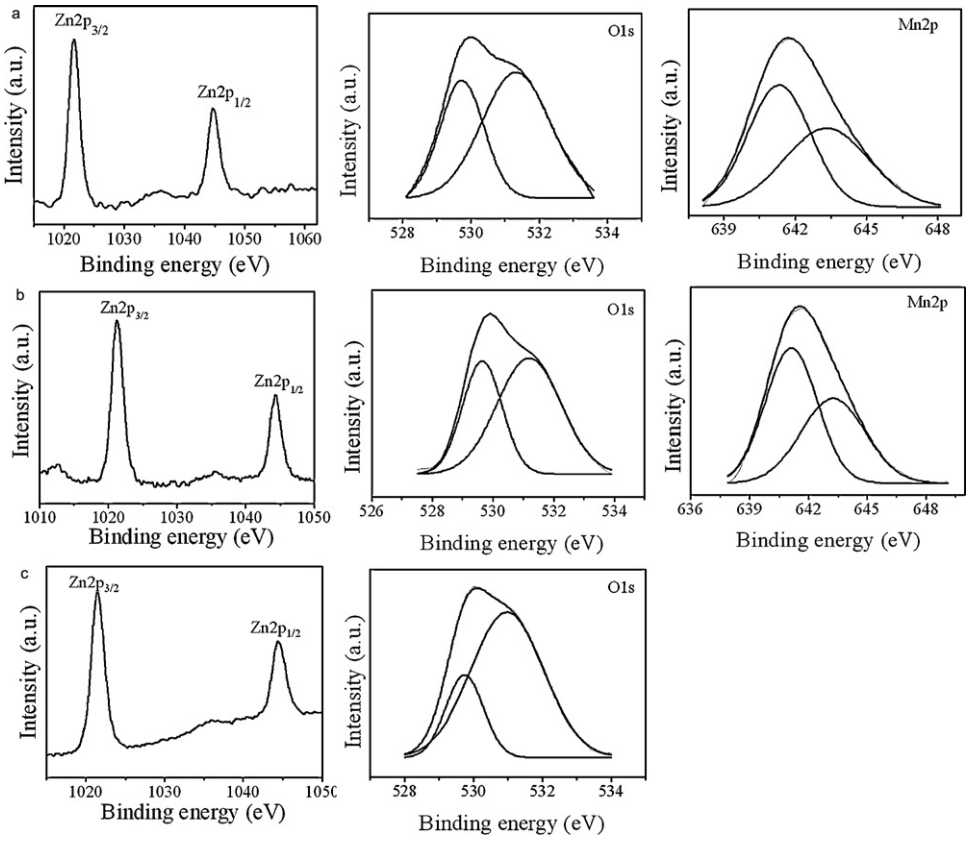

Fig. 3. XPS spectra for RTA annealed Mn:ZnO nanorod-films showing core level peaks corresponding to Zn 2p, O 1s and Mn 2p for: (a) Mn:ZnO (Mn ~ 2.6 at%); (b) Mn:ZnO (Mn ~ 4.8 at%) and (c) pure ZnO nanorods.

the Mn:ZnO films were computed from the XRD patterns for the annealed films and are shown in Table 1. It may be seen that the lattice constants of pure ZnO nanorods agreed well with the bulk values (a = 0.32495 nm; c = 0.52069 nm) [19]. Both the 'a' and the 'c' values increased slightly with the increased incorporation of Mn in the ZnO nanorods as shown in Table 1.

At this juncture, it will be prudent to examine the possible charge states of Mn existing in these Mn: ZnO nanorod films and it will also be pertinent enough to carry out XPS and Raman studies in these films. It may be noted here that the results presented in the subsequent sections will refer to the annealed samples only, unless stated otherwise.

3.2. XPS analysis

The binding states of the compositional elements of Mn:ZnO nanorods were characterized by XPS studies. Fig. 3(a) and (b) shows the typical core level peaks corresponding to Zn 2p, O 1s and Mn 2p of the Mn:ZnO nanorods for two representative films with different amounts of Mn incorporated in them. The Mn $2p_{3/2}$ peak of Mn:ZnO nanorods located at 643.2 eV is not as asymmetric as compared to that for oxygen (Fig. 3(a) and (b)). It deviated significantly from a Gaussian distribution. The Mn $2p_{3/2}$ peak of Mn:ZnO nanorods located at 643.2 eV could be deconvoluted in two peaks located at ~641.4 and 643.3 eV, which could be attributed to the existence Mn^{2+} and Mn^{4+}, respectively [20]. It is well known that, for one kind of element, its ion with a high valence has a larger binding energy than its low valence ion. Generally, peaks for the metallic Mn and Mn^{4+} ion are located at 637.7 eV and 642.4 eV as indicated in Ref. [21]. It may be mentioned here that an extra high-energy feature at ~644.6 eV in the Mn 2p XPS spectra as observed by Cong et al. [22] was attributed to ligand to metal charge transfer *shake-up* transitions. We have computed the peak areas of the different valence bonds of Mn and the ratios of Mn^{2+}/Mn^{4+} in each sample were computed by using the relation:

$$\frac{n(E1)}{n(E2)} = \frac{A(E1)/S(E1)}{A(E2)/S(E2)}$$

where n is the number of element atom, A is the area of the XPS peak of the element, E is the element and S is the elemental sensitivity factor. The ratios of Mn^{2+}/Mn^{4+} computed as above are shown in Table 1. It was found that the atomic concentration of Mn^{2+}, in all the samples increased with increased amount of Mn incorporation in the ZnO lattice. Also the atomic concentration of Mn^{2+} was found to be large as compared to the atomic concentration of Mn^{4+} for all the samples.

The O 1s peaks with their deconvolution result for two representative Mn incorporated ZnO are shown in Fig. 3(a) and (b), respectively. The peaks for O 1s could be deconvoluted by curve fitting method in two Gaussian peaks centered at ~529.6 eV and ~531.2 eV. The high binding energy component centered at 531.2 eV can be ascribed to the chemisorbed oxygen of the surface hydroxyl, $-CO_3$, absorbed H_2O or absorbed O_2 [23], which cannot be easily removed. The component with low binding energy centered at 529.6 eV could be attributed to the O^{2-} ions in the ZnO lattice. For the sake of comparison, the XPS spectra of pure ZnO nanorods are also appended here (Fig. 3(c)). The deconvoluted O 1s peaks could be seen centered at ~529.7 eV and ~530.9 eV. Both the peaks have the binding energies shifted slightly towards lower energy. The value of Zn/O ratio computed from the above spectra is ~1.11. The intensity of this peak would indicate the amount of oxygen atoms in the wurtzite structure of the hexagonal Zn^{2+} ion array.

The XPS spectrum of Zn 2p peak (Fig. 3) exhibited the characteristic doublet corresponding to the peak at ~1021.8 eV for Zn $2p_{3/2}$ and at ~1044.8 eV for Zn $2p_{1/2}$. Due to the ion radii difference between Mn^{2+} (0.66 Å) and Zn^{2+} (0.60 Å), Mn with larger ionic radius replacing Zn of the ZnO lattice could result in the increasing binding energy of Zn. This explains the slightly higher energy position of the peak centered at 1021.8 eV than that of Zn in the bulk ZnO (1021.4 eV). The effective concentrations of Mn^{2+} incorporated into the films are found to be ~2.6 at%, ~4.3 at% and ~4.8 at% corresponding to Mn layer thickness of 3 nm, 6 nm and 10 nm, respectively, for the ZnO-nanorod samples. Relative amounts of Mn:Zn are shown in Table 1.

Although, the XPS results showed that Mn^{2+} state was the dominant charge state, but it may be stressed here that elemental quantification made by proton-induced X-ray emission (PIXE) and Rutherford back scattering spectrometry (RBS) measurements would have yielded more authentic information of the quantification and distribution of Mn throughout the ZnO nanorods [24,25]. PIXE is highly sensitive to elemental analysis and thus is an excellent technique to quantify the overall concentration of host as well as dopant materials. The X-ray yield of Mn and Zn would have affirmed that Mn atoms were located on substitutional Zn lattice sites. Additionally, the RBS spectra would have illustrated both crystalline quality and orientation. The authors regret to indicate that due to unavailability of the above supporting equipments in the University, they are unable to include more authentic information on Mn^{2+} ions in ZnO lattice as an additional support to the information obtained by XPS measurements.

3.3. Raman analysis

Among the other techniques, Raman spectroscopy offers a non-destructive tool for obtaining information about both the local and the non-local vibrational states related to the structure of ZnMnO compounds. Typical Raman spectra of three representative as-deposited Mn:ZnO nanorod films grown on glass substrates are shown in the insets of Fig. 4(a)–(c). All the spectra are dominated by the presence of a strong peak located at ~438 cm^{-1} followed by peaks at ~332 cm^{-1} and 378 cm^{-1} (unmarked) in the low wavelength number region. There is only one peak at ~577 cm^{-1} in the higher wave number region. The peak at ~438 cm^{-1} may be identified as high frequency branch of E_2 mode of ZnO. The broad and asymmetric nature of this peak is typical of the Raman active mode specially observed in wurtzite structure. The peak at ~577 cm^{-1} could be attributed to the A_1 longitudinal optical (LO) mode of ZnO. Origin of the above modes may be due to Zn interstitials present in the films. The second order Raman arising from the E_2 (high) − E_2 (low) multiple scattering processes appeared at ~332 cm^{-1}. This observation is in conformity with that observed by Gao et al. [26] from their studies on ZnO nanorods deposited by solution deposition method on GaN wafer. A very low intensity peak at ~378 cm^{-1} present (inset of Fig. 4(b) and (c); not marked) in the Raman spectra for as-deposited Mn:ZnO nanorods could be identified as arising out of A_1 Raman vibration modes. The appearance of Raman peaks at ~438 cm^{-1} and ~378 cm^{-1} is in conformity with the observation by Wu et al. [27] on the ZnO nanowires prepared via sol–gel template route by them.

When the above as-deposited Mn:ZnO films were subjected to RTA, a drastic change in the Raman spectra is observed (Fig. 4(a)–(c)). The Raman spectra of the annealed Mn:ZnO nanorods indicated only one characteristic peak at ~438 cm^{-1} for Mn:ZnO films with lower Mn content (Fig. 4(a)). Films containing higher Mn content indicated an additional Raman feature located at ~660 cm^{-1}. We did not observe any peak at ~522 cm^{-1} as was observed by Yang et al. [28], the origin of which was associated with

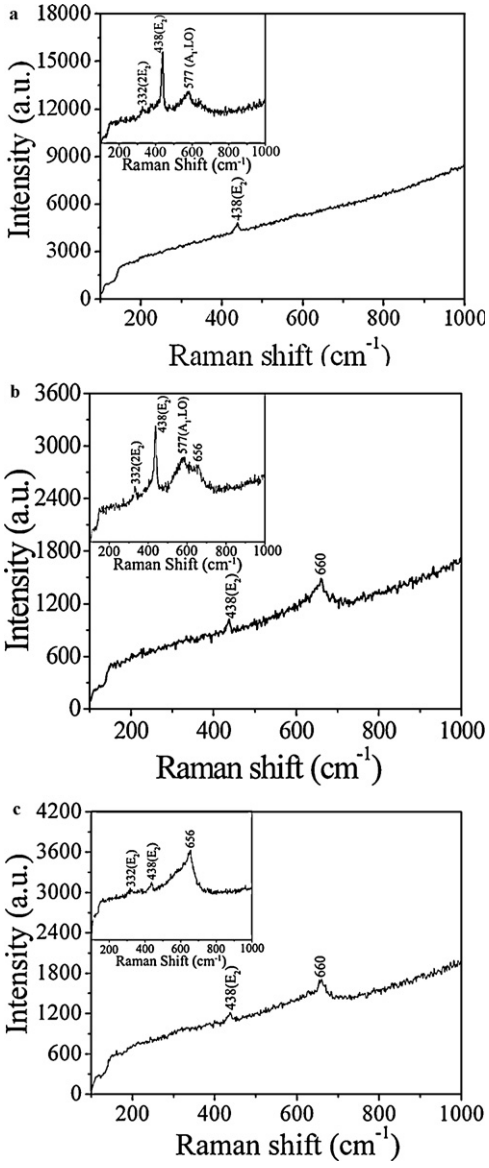

Fig. 4. (a) Raman spectra for RTA annealed Mn:ZnO nanorod-films: (a) Mn:ZnO (Mn ~ 2.6 at%); (b) Mn:ZnO (Mn ~ 4.3 at%); (c) Mn:ZnO (Mn ~ 4.8 at%). Insets show the Raman spectra for as-deposited Mn:ZnO films.

Mn doping. Disappearance of the Raman peak at ~577 cm^{-1} in the annealed films, arising due to the Zn interstitials, may be related to the substitution of Mn^{2+} in the Zn^{2+} site with annealing. Xu et al. [29] and Kim and Stair [30] observed the existence of a weak peak at about 665 cm^{-1} which was ascribed to the vibration mode of Mn–O. In the present study, the observed vibrational mode at ~660 cm^{-1} in Mn:ZnO nanorod samples appeared only for samples containing higher amount of Mn. Yang et al. [28] indicated that the vibration mode at ~660 cm^{-1} may be ascribed to an intrinsic mode of ZnO related to oxygen vacancies (V_o), zinc interstitials (Zu_{ni}), anisette oxygen, etc. However, Samanta et al. [31] also observed additional modes at ~680 cm^{-1} and attributed the origin of this peak to the precipitation of spinal secondary phase $ZnMn_2O_4$ in 10% Mn doped ZnO. We have not observed the presence of any secondary phase $ZnMn_2O_4$ in the XRD traces in any of our samples and moreover the amount of Mn present in the samples under this study was significantly lower. Thus, we apprehend that this Raman peak at ~660 cm^{-1} did not originate from possible partial formation of Mn-rich solid solution layer in the Mn:ZnO nanorods or precipitation of

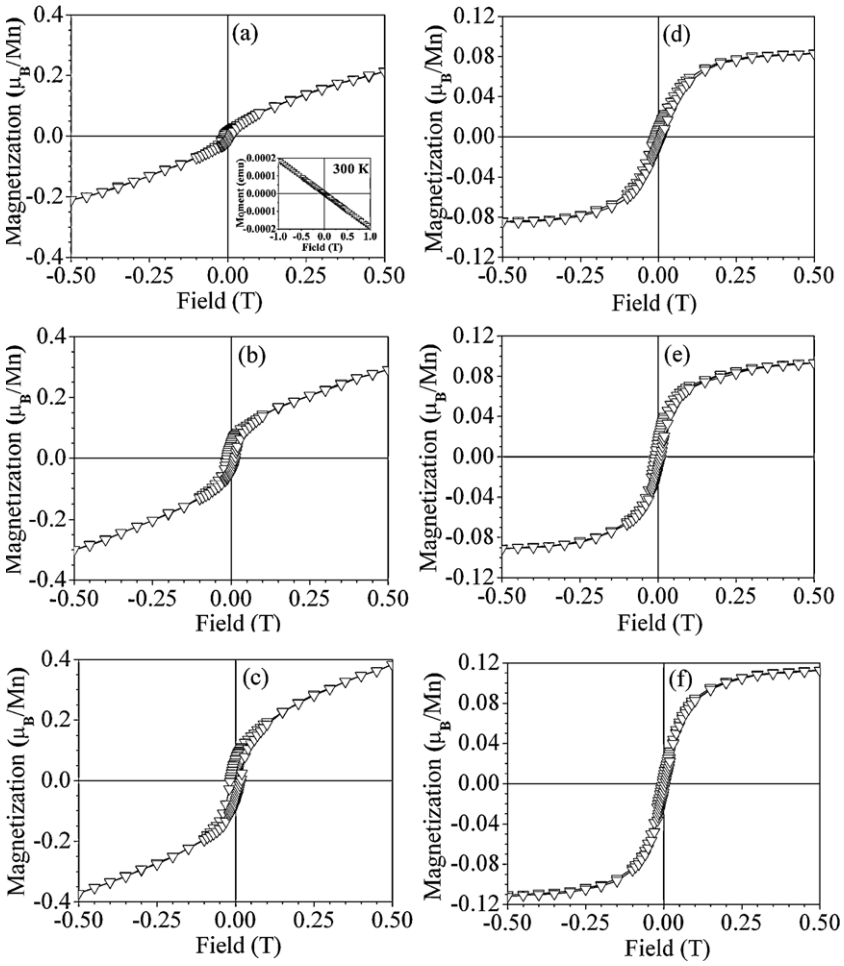

Fig. 5. *M–H* curves for RTA annealed Mn:ZnO nanorod-films: at 35 K for (a) Mn:ZnO (Mn ~ 2.6 at%) (Inset: *M–H* curve for pure ZnO nanorods film); (b) Mn:ZnO (Mn ~ 4.3 at%); and (c) Mn:ZnO (Mn ~ 4.8 at%); and at 300 K for (d) Mn:ZnO (Mn ~ 2.6 at%), (e) Mn:ZnO (Mn ~ 4.3 at%) and (f) Mn:ZnO (Mn ~ 4.8 at%).

$ZnMn_2O_4$. Rather, this peak might have originated from the combined effect of two-phonon signal of ZnO as indicated by Calleja and Cardona [32] and Hasuike et al. [33] and the vibration mode of Mn–O as observed by Xu et al. [29].

3.4. Magnetization studies

M–H hysteresis curves recorded at 35 K and 300 K for the Mn:ZnO nanorod-films containing different amounts of Mn are shown in Fig. 5(a)–(c) and (d)–(f), respectively, which clearly indicated that the films are ferromagnetic. The magnetic field was applied parallel and perpendicular to the substrate of Mn:ZnO nanorod-film and measurements were carried out in both the configurations. It may be noted here that no significant change was observed in the magnetic behavior when measured in the above configurations. The magnetization values were systematically a bit higher in parallel configuration than that measured in perpendicular configuration. Thus the results presented here will represent the magnetic measurements carried out in parallel configuration only.

The saturation magnetization (M_S) of the Mn:ZnO nanorod-films consistently increased with Mn concentration. The M_S of the films are estimated to be 0.21, 0.29, 0.38 b_e/Mn at 35 K and 0.083, 0.093, 0.11 b_e/Mn at room temperature (300 K). *M–H* data showed that magnetization decreased with increase in temperature. It was observed clearly from the expanded view of the *M–H* curves (not shown here) that the values of the coercive fields measured under both increasing (H_{C+}) and decreasing fields (H_{C-}) are nearly the same. The values of coercive fields (H_e) obtained as above at 35 K and 300 K have been tabulated in Table 1. A variation of $\Delta H [= |(H_{C+}) - (H_{C-})|]$ for all the films with different Mn contents revealing the differences in the coercive fields is indicated in Fig. 6. Variation of this difference (ΔH) did not indicate any significant change for films containing increased amount of Mn particles in the ZnO matrix. This would indicate that the possible presence of increased manganese oxides due to surface oxidation (if any), in these films, contributing to the modulation of the magnetic properties of these films, was absent. On the contrary, the oxide surface layers might have resulted in ferromagnetic sub-phases (especially

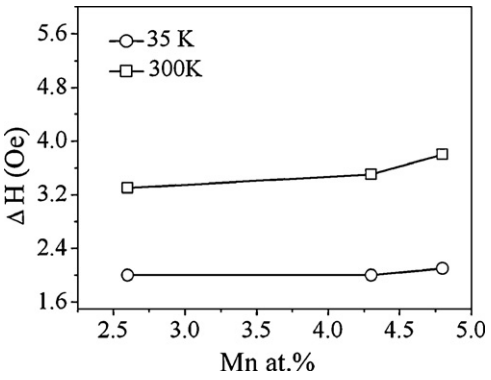

Fig. 6. Variation of coercive field difference (ΔH) with the Mn content in the ZnO nanorod films.

Mn_3O_4) and which would not contribute to the observed ferromagnetism at room temperature as it has a Curie temperature ~43 K [34]. Moreover, the other manganese oxides (MnO and MnO_2) are well known antiferromagnets below their respective Neel temperature of 116 K and 84 K. These oxide surface layers (if present) would have resulted in a shell-core morphology wherein an antiferromagnetic oxide layer would surround the Mn^{2+} influencing the magnetic properties due to the exchange interaction between the ferromagnetic and the antiferromagnetic phases. Thus, a significant difference in coercive fields could have been observed due to the presence of surface manganese oxide layer resulting in the exchange bias. Similar observation was made for metallic nanoparticles with shell NiO/core Ni morphology, which supported the presence of oxide surface layers [35,36]. The residual magnetization also gradually increased for films containing increased amount of manganese particles. It may be noted here that pure ZnO nanorods did not show any ferromagnetic properties as is evident from the *M–H* plot shown in the inset of Fig. 5(a). Thus, the above results confirm that Mn doping in ZnO lattice would induce ferromagnetic ordering at room temperature.

The magnetization due to spin-split donor impurity band is generally very anisotropic [37] in crystalline materials, with variations up to a factor of 3 depending on the orientation of the applied field relative to the substrate. Also, there is not much difference in magnetization in parallel and perpendicular configurations. Thus, it may possibly imply that bound magnetic-polaron may dominate magnetic exchange interaction and as such the origin of magnetism in our samples may be related to the bound magnetic polarons.

The magnetization results for the Mn-implanted nanorods are very similar to those reported previously for Mn-implanted, bulk *n*-type ZnO single crystals, in which high resolution X-ray diffraction showed no secondary phases [38]. We note also that the solubility limits for Mn in ZnO are between 13% for equilibrium conditions and 35% for incorporation by pulsed laser deposition [5]. These values are well beyond the concentrations employed here. Thus, the observed ferromagnetic behavior could be attributed to the substitution of Mn ions (Mn^{2+}) for Zn ions in the ZnO lattice. This observation is in conformity with that reported by Lin et al. [21] and Cong et al. [22]. According to the results of XRD, XPS, Raman spectra and the magnetic properties, it may be concluded that the Mn^{2+} played the most important role in the ferromagnetic properties of Mn-doped ZnO [39]. According to RKKY theory [40,41], the magnetism is due to the exchange interaction between local spin-polarized electrons (such as the electrons of Mn^{2+} ions) and conductive electrons. This interaction leads to the spin polarization of conductive electrons. Subsequently, the spin-polarized conductive electrons perform an exchange interaction with local spin-polarized electrons of other Mn^{2+} ions. Thus after the long-range exchange interaction, almost all Mn^{2+} ions exhibit the same spin direction. The conductive electrons are regarded as a medium to contact all Mn^{2+} ions. As a result, the material exhibits ferromagnetism. However, direct Mn–Mn interactions have been used to explain anti-ferromagnetism by some researchers [17]. XPS studies indicated that incorporated Mn was in Mn^{2+} and Mn^{4+} states. Mn^{2+} atomic concentration was found to be larger than Mn^{4+} concentration in all the samples. Also, disappearance of the Raman peak at ~577 cm^{-1} arising due to the Zn interstitials may be related to the substitution of Mn^{2+} in the Zn^{2+} site with annealing. Additionally, pure ZnO nanorods did not indicate any ferromagnetic behavior. It may be noted here that the largest magnetic moment obtained in this study was ~0.11 μ_B/Mn which is smaller that commonly obtained value of 5.9 μ_B/Mn^{2+}. This would imply that not all Mn ions took part in ferromagnetic behavior in these films. Also, when the uncorrelated spins, responsible for paramagnetic component are taken into account for computing magnetic moment, the resultant moment per Mn ion would indicate higher values. This may be the basic cause of obtaining lower values of magnetic moment in our films. Thus, it may be concluded from this study that Mn metal inclusions as Mn^{2+} in the ZnO lattice are possibly responsible for such existence of magnetic moment in the films as no phase of Mn_3O_4 could be detected from our XRD and XPS results. The XRD, XPS and Raman results implied that most Mn ions were located at Zn sites, and the occupation rate of Mn^{2+} ions at the Zn sites would increase with increasing Mn incorporation.

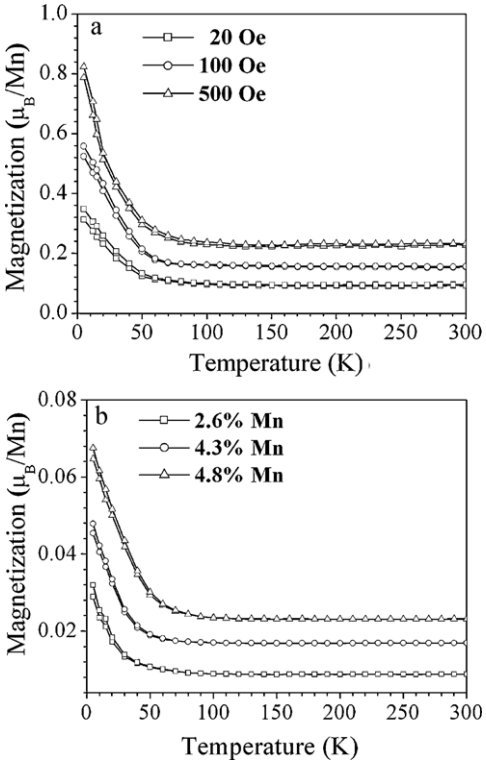

Fig. 7. (a) Temperature dependence of magnetization (*M–T*) curve for a representative Mn:ZnO (Mn ~ 4.8 at%) sample in ZFC and FC conditions in the presence of dc magnetic fields of 20, 100 and 500 Oe. (b) Temperature dependence of magnetization for Mn:ZnO films with different Mn contents in ZFC and FC conditions in the presence of dc magnetic field of 20 Oe.

Fig. 7(a) presents the zero-field cooling (ZFC) and field-cooling (FC) *M–T* curves of representative sample Mn:ZnO film (Mn ~4.8 at%) from 2 K to 300 K at applied fields of 20 Oe, 100 Oe, and 500 Oe. Variation of magnetization with temperature for Mn:ZnO films containing different Mn contents is shown in Fig. 7(b). The contribution from the glass substrate was subtracted from the raw data. Magnetization could be seen to increase rapidly below 50 K for all the films measured at different magnetic fields (Fig. 7(a)). The sample shows ferromagnetic behavior persisting above 300 K and T_C is thus estimated to be higher than 300 K. Magnetization measured at H = 20, 100 and 500 Oe was found to be essentially temperature independent between 35 and 300 K with no difference in either the ZFC and FC case. Thus, it indicated the magnetization existed up to room temperature. This is in agreement with the results reported by others [42,43] which led to the suggestion of room temperature ferromagnetism. A model [44] combining both paramagnetic and ferromagnetic components may account for the initial decrease of magnetization from 2 K to 35 K and remaining non-zero up to 330 K. No signature of superparamagnetic blocking temperature (T_B) peak could be observed in the ZFC magnetization data. The blocking may be present in the nanorods but may not be observed because of very small particle size. The small particle size leads to very low T_B well below the detection limit of SQUID magnetometer [45].

4. Conclusions

In conclusion, aligned nanorods of Mn:ZnO (Mn = 2.6–4.8 at%) was synthesized by hybrid wet chemical route on glass substrates and the microstructural, chemical compositional and magnetic properties were investigated. Room temperature ferromagnetic ordering for the Mn:ZnO nanorods were clearly observed. The Curie temperature for all the nanorod films is above room temperature. Pure ZnO nanorods did not show any ferromagnetic properties. The magnetization increases with Mn doping in ZnO nanorods ($0.083 \leq M_S \leq 0.11\ \mu_B$/Mn). XPS studies indicated that incorporated Mn was in Mn^{2+} and Mn^{4+} states. Mn^{2+} atomic concentration was found to be larger than Mn^{4+} concentration in all the samples. Disappearance of the Raman peak at $\sim$577 cm^{-1} arising due to the Zn interstitials may be related to the substitution of Mn^{2+} in the Zn^{2+} site with annealing. Thus, Mn metal inclusions as Mn^{2+} in the ZnO lattice are possibly responsible for such large magnetic moment at room temperature in the films.

Acknowledgements

MKS would like to thank Council of Scientific and Industrial Research (CSIR), India for the award of Senior Research Fellowship. RNG wishes to thank Coal S&T, Ministry of Coal, Government of India, for granting him fellowship. Authors would like to thank DST SQUID facility at Indian Institute of Technology, Delhi. Thanks are also due to Dr. S. Verma, Institute of Physics, Bhubaneswar, India, for her kind help in recording the XPS spectra.

References

[1] S.A. Wolf, D.D. Awschalom, R.A. Buhrman, J.M. Daughton, S. vonMolnar, M.L. Roukes, A.Y. Chtchelkanova, D.M. Treger, Science 294 (2001) 1488.
[2] T. Dietl, H. Ohno, F. Matsukura, J. Cibert, D. Ferrand, Science 287 (2000) 1019.
[3] Y.Z. Yoo, T. Fukumura, Z. Jin, K. Hasegawa, M. Kawasaki, P. Ahmet, T. Chikyow, H. Kainuma, J. Appl. Phys. 90 (2001) 4246.
[4] M.H. Kane, K. Shalini, C.J. Summers, R. Varatharajan, J. Nause, C.R. Vestal, Z.J. Zhang, I.T. Ferguson, J. Appl. Phys. 97 (2005) 023906.
[5] T. Fukumura, Z. Jin, M. Kawasaki, T. Shono, T. Hasegawa, S. Koshiharan, H. Koinuma, Appl. Phys. Lett. 78 (2001) 958.
[6] P. Amézaga-Madrid, W. Antúnez-Flores, J.E. Ledezma-Sillas, J.G. Murillo-Ramírez, O. Solís-Canto, O.E. Vega-Becerra, R. Martínez-Sánchez, M. Miki-Yoshida, J. Alloys Compd. (2011), doi:10.1016/j.jallcom.2011.01.044.
[7] S.W Jung, S.-J. An, G.-C. Yi, C.U. Jung, S.-I. Lee, S. Cho, Appl. Phys. Lett. 80 (2002) 4561.
[8] Z.-W. Jin, Y.-Z. Yoo, T. Sekigushi, T. Chikyow, H. Ofuchi, H. Fujioka, M. Oshima, H. Koinuma, Appl. Phys. Lett. 83 (2003) 39.
[9] P. Sharma, A. Gupta, K.V. Rao, F.J. Owens, R. Sharma, R. Ahuja, J.M. Osorio Guillen, B. Johansson, G.A. Gehring, Nat. Mater. 2 (2003) 673.
[10] J. Han, P.Q. Mantas, A.M.R. Senos, J. Eur. Ceram. Soc. 49 (2002) 22.
[11] J. Wang, W. Chen, M. Wang, J. Alloys Compd. 449 (2008) 44.
[12] K.J. Kim, Y.R. Park, J. Appl. Phys. 94 (2003) 867.
[13] A.B. Mahmound, H.J. von Bardeleben, J.L. Cantin, A. Mauger, E. Chikoidze, Y. Dumont, Phys. Rev. B 74 (2006) 115203.
[14] S.-H. Hu, Y.-C. Chen, C.-C. Hwang, C.-H. Peng, D.-C. Gong, J. Alloys Compd. 500 (2010) L17.
[15] L. Liao, W.F. Zhang, H.B. Lu, J.C. Li, D.F. Wang, C. Liu, D.J. Fu, Nanotechnology 18 (2007) 225.
[16] R.N. Gayen, S. Dalui, A. Rajaram, A.K. Pal, Appl. Surf. Sci. 255 (2009) 4902.
[17] H. Ohno, Science 281 (1998) 951.
[18] S.J. Pearton, C.R. Abernathy, D.P. Norton, A.F. Hebard, Y.D. Park, L.A. Boatner, J.D. Budai, Mater. Sci. Eng. Rep. 40 (2003) 137.
[19] O. Madelung, M. Schulz (Eds.), Landolt-Bornstein New Series, Subvolume a, vol. 22, Springer-Verlag, Berlin, 1987.
[20] J.F. Moulder, Handbook of X-ray Photoelectron Spectroscope, Perkin-Elmer Corporation, Eden Prairie, 1979, p. 226.
[21] Y.B. Lin, J.P. Xu, W.Q. Zou, L.Y. Lv, Z.H. Lu, F.M. Zhang, Y.W. Du, Z.G. Huang, J.G. Zheng, J. Phys. D: Appl. Phys. 40 (2007) 3674.
[22] C.J. Cong, L. Liao, Q.Y. Liu, J.C. Li, K.L. Zhang, Nanotechnology 17 (2006) 1520.
[23] J.H. Li, D.Z. Shen, J.Y. Zhang, D.X. Zhao, B.S. Li, Y.M. Lu, Y.C. Liu, X.W. Fan, J. Magn. Magn. Mater. 302 (2006) 118.
[24] M. Diaconu, H. Schmidt, H. Hochmuth, M. Lorenz, G. Benndorf, D. Spemann, A. Setzer, P. Esquinazi, A. Pöppl, H. von Wenckstern, K.-W. Nielsen, R. Gross, H. Schmid, W. Mader, G. Wagner, M. Grundmann, J. Magn. Magn. Mater. 307 (2006) 212.
[25] W.M. Hlaing Oo, L.V. Saraf, M.H. Engelhard, V. Shutthanandan, L. Bergman, J. Huso, M.D. McCluskey, J. Appl. Phys. 105 (2009) 013715.
[26] H. Gao, F. Yan, J. Li, Y. Zeng, J. Wang, J. Phys. D: Appl. Phys. 40 (2007) 3654.
[27] G.S. Wu, T. Xie, X.Y. Yuan, Y. Li, L. Yang, Y.H. Xiao, D.L. Zhang, Solid State Commun. 134 (2005) 485.
[28] L.W. Yang, X.L. Wu, G.S. Huang, T. Qiu, Y.M. Yang, J. Appl. Phys. 97 (2005) 014308.
[29] C.X. Xu, X.W. Suna, Z.L. Dong, S.T. Tan, Y.P. Cui, B.P. Wang, J. Appl. Phys. 98 (2005) 113513.
[30] H.S. Kim, P.C. Stair, J. Phys. Chem. B 108 (2004) 17019.
[31] K. Samanta, S. Dussan, R.S. Katiyar, P. Bhattacharya, Appl. Phys. Lett. 90 (2007) 261903.
[32] J.M. Calleja, M. Cardona, Phys. Rev. B 16 (1977) 3753.
[33] N. Hasuike, R. Deguchi, H. Katoh, K. Kisoda, K. Nishio, T. Isshiki, H. Harima, J. Phys.: Condens. Matter. 19 (2007) 365223.
[34] S.J. Pearton, W.H. Heo, M. Ivill, D.P. Norton, T. Steiner, Semicond. Sci. Technol. 19 (2004) R59.
[35] M. Fraune, U. Rudiger, G. Guntherodt, S. Cardoso, P. Freitas, Appl. Phys. Lett. 77 (2001) 3815.
[36] F.C. Fonseca, A.S. Ferlauto, F. Alvarez, G.F. Goya, R.F. Jardin, J. Appl. Phys. 97 (2005) 044313.
[37] M. Venkatesan, C.B. Fitzgerald, J.G. Lunney, J.M.D. Coey, Phys. Rev. Lett. 93 (2004) 177206.
[38] D.P. Norton, S.J. Pearton, A.F. Hebard, N. Theodoropoulou, L.A. Boatner, R.G. Wilson, Appl. Phys. Lett. 82 (2003) 239.
[39] C.J. Cong, L. Liao, J.C. Li, L.X. Fan, K.L. Zhang, Nanotechnology 16 (2005) 981.
[40] M.A. Ruderman, C. Kittel, Phys. Rev. 96 (1954) 99.
[41] K. Yosida, Phys. Rev. 106 (1957) 893.
[42] Y. Matsumata, M. Urakami, T. Shono, T. Hasegawa, T. Fukumura, M. Kawasaki, P. Ahmet, T. Chikyow, S.-Y. Koshihara, H. Koinuma, Science 291 (2001) 854.
[43] S.A. Chambers, S. Thevuthasan, R.F.C. Farrow, R.F. Marks, J.U. Thiele, L. Folks, M.G. Samant, A.J. Kellock, N. Ruzycki, D.L. Ederer, U. Diebold, Appl. Phys. Lett. 79 (2001) 3467.
[44] J.C.A. Huang, H.S. Hsu, Y.M. Hu, C.H. Lee, Y.H. Huang, M.Z. Lin, Appl. Phys. Lett. 85 (2004) 3815.
[45] R. Goswami, G. Kioseoglou, A.T. Hanbicki, O.M.J. van't Erve, B.T. Jonker, G. Spanos, Appl. Phys. Lett. 86 (2005) 032509.